Journal Name

ARTICLE

Enhancing Cycling Durability of Li-ion Batteries with Hierarchical Structured Silicon-Graphene Hybrid Anodes

Received 00th January 20xx,
Accepted 00th January 20xx

DOI: 10.1039/x0xx00000x

www.rsc.org/

Melanie J. Loveridge [a], Michael J. Lain, Qianye Huang, Chaoying Wan, Alexander J. Roberts, George S. Pappas and Rohit Bhagat.

Hybrid anode materials consisting of micro-sized silicon (Si) interconnected with few-layer graphene (FLG) nanoplatelets and sodium-modified poly (acrylic acid) (PAA) as a binder were evaluated for Li-ion batteries. The hybrid film has demonstrated a reversible discharge capacity of ~1800 mAh/g with a capacity retention of 97% after 200 cycles. The superior electrochemical properties of the hybrid anodes are attributed to a durable, hierarchical conductive network formed between Si particles and the multi-scale carbon additives, with enhanced cohesion by the functionalized polymer binder. Furthermore, improved SEI stability is achieved from the electrolyte additives, due to the formation of a kinetically stable film on the surface of the Si.

Introduction

The continued global drive for a clean energy future is a compelling driving force motivating research groups across the world. This is especially true in the electrification of transport, if this is to be a viable strategy for reducing oil dependency and the associated environmental impacts of road transportation. In parallel, to enable the increased generation of renewable electricity by way of the grid, static storage solutions will be of equal, high impact. For the successful electrification of vehicles and effective, long-term grid storage opportunities batteries are required to last much longer and deliver energy at a higher rate than is currently possible.

Critical here are the Li-ion chemistries that need to be made from electrode materials of reasonable cost, safety (non-toxic, excellent structural/chemical stability with low heat generation), long cycle life and abundance – the key factors to address the Li-ion energy storage "*quadrilemma*" as depicted in Figure 1.

From an energy density perspective silicon (Si) has been the focus of much research due to its considerable capacity of 3579 mAh/g, second only to lithium metal [1]. However, its obvious drawbacks have highly limited its performance and applications, such as the significant volume expansion upon lithiation, low conductivity and consumption of Li ions by the way of continued SEI growth [2,3].

The volume expansion is around 280 % at maximum capacity (3579 mA h/g), and around 100 % at more practical capacities (1200 mA h/g). This imposes serious mechanical challenges to the electrode before any further electrochemical processes associated with SEI growth and cracking. . In comparison, graphite anodes have dominated the electrode chemistry since the launch of LIBs due to its high electrical conductivity and low cost, but their limited capacity of 372 mAh/g simply hinders further development for transport applications.

[a] *Energy Innovation Centre WMG, Warwick University, CV5 7AL*
† Corresponding Author UK email: m.loveridge@warwick.ac.uk.

Figure 1 The Li-Ion Energy storage "quadrilemma"

.

Attempts to improve the electrochemical performance of Si materials have been based mainly on using nanostructured Si materials, nanoporous Si frameworks as well as core-shell / hollow Si structures [4]. Nanostructured Si materials (<150 nm) may release strain more effectively and thus experiences less structural damage and pulverisation upon lithiation as compared to bulk Si [5]. However, the drawbacks of incorporating nano-sized Si as the anode active material are obvious: (i) a higher surface area (≥100 m^2/g) resulting in a larger initial SEI film growth, (ii) electrochemical sintering processes are not avoidable, emanating from localised spikes in current / voltage which leads to performance deterioration.

In addition to active particles, the choice of polymeric binders is considered to be critical to the performance of Si anodes. Effective binders are those that can meet the following criteria: (a) adhesion between the electrode and the current collector (b) interface integrity between polymer and active material surface (c) interaction of the polymer with electrolyte solvents and (d) the tensile mechanical properties The frequently used polymers such as PAA), as shown in Figure 2 [6], sodium carboxymethyl cellulose (Na-CMC) [7] and polyimide (PI) [8], have shown effective binding functions due to their abundant functional groups. In Figure 2 the interaction of the polymer carboxyl groups with the native oxide-containing groups is illustrated

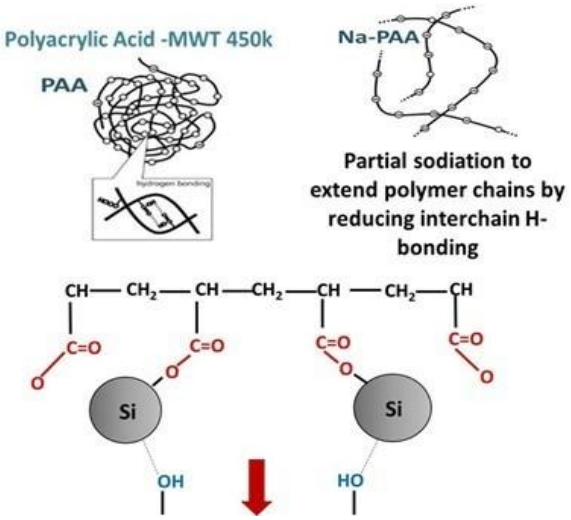

Figure 2 An illustration of sodium-modified poly (acrylic acid) and its interaction with Si particle [9].

Apart from polymer binders, often two or more types of conductive carbon are used to provide multi-scale conducting network, such as small particles like acetylene black combined with larger particles with higher aspect ratio e.g. vapour-grown carbon fibre (longer range). This is carried out to highly promote the conducting network formation and enhance the rate performance of the anodes. Graphene has attracted considerable research effort on its combination with Si in anodes [10,11]. The desirable properties associated with graphene, namely superior in-plane electrical conductivity, high surface area and excellent mechanical properties,

make it an interesting conductive additive for a more durable anode architecture.

The theoretical capacity has been cited as 740-780 mAh/g, which is approximately twice that of graphite, and in addition it is postulated that the diffusion pathway of the lithium ions will be less tortuous [12].

In this study, we will exploit the conductive and mechanical properties of FLG graphene to engineer electrodes with more uniform conductive pathways and to protect against degradation.

It has been found that the electronic structure of few-layer graphene (<10 layers) is different from that of bulk graphite, in light of this it is useful to precisely define the different types of graphene possible, i.e. single layer graphene, bilayer graphene and few-layer graphene (FLG) [13].

Differential capacity analysis (dQ/dV) is used in this study and is the first derivative of the galvanostatic curve and shows a series of peaks that correspond to plateaus as seen in the respective voltage profiles. Analysis using dQ / dV has been used on a number of lithium ion battery chemistries [14–16]. For dQ/dV vs. voltage plots, the peaks correspond to specific processes relating to phase equilibria and are voltage-specific.

Experimental

Silicon electrodes were prepared following the procedures as described below.

Stock PAA solution

Polyacrylic acid (PAA; Sigma Aldrich, MWT = 450k, purity ≥ 99.5%) aqueous solution (12wt %) was prepared using a Primix Homodisper (Model 2.5) at room temperature. Then 0.12 mol of sodium carbonate (Na_2CO_3; Fisher Chemical, purity > 99.5 %) was added to form partially neutralise Na-PAA solution.

Carbon composite solution*:*

Carbon composite formulation: 10g few-layer graphene (FLG, XG Sciences) is dry-blended with 5 g acetylene black (Alfa Aesar) on a roller blender for 30 minutes. 135.9g deionised water containing 0.1g polyacrylic acid (Acros Organics) is added to the carbon blend and the resulting suspension is high-shear stirred for 1 hour at 500rpm. The resulting slurry is then dispersed further ultrasonically using a Hielscher 400 UPS (400W, 24Hz) sonotrode in static mode with an amplitude of 60% at 0.5 cycles for 15 minutes. This generates an effectively dispersed mixture of hierarchical carbons as shown in Figure 2.

Si Composite Electrode Formulation

20 g of Si (Elkem Silgrain e-Si, d_{50} 3.1 µm, purity 99.7%) is mixed with 43.6 g of the C-mix (107.1g wt% solids mass) in a nalgene vessel – Si particle morphology can be seen in Figure 3. The Si composite slurry is then subjected to Ultrasonication to break down any Si / C agglomerates. After sonication the slurry is further mixed using medium sheer stirring in a Primix Homodisper Model 2.5 for 30 minutes at 1000 rpm. 33.33 g of the partially neutralized Na-PAA solution (conc.12% w/v) is added to all of the Si slurry described above. The composite slurry is further dispersed using a Primix Homodisper Model 2.5 for 30 minutes. 30 mL of the resulting solution is transferred to a Filmix mixing vessel and subjected to the following mix cycle in a Filmix™ Thin-film Disperser Model 40-60: two dispersions for 30 s each at 10 m/s then 30 s at 25 m/s. The rest of the slurry receives the same mixing procedure (the solution was broken up into two smaller batches to accommodate the 60 mL

volume of the Filmix mixing vessel. The above formulations result in electrodes with dry mass % composition of 56: 20: 14: 10 (Si: FLG: PAA: Acetylene black). A control anode (containing no graphene) is formulated based on a dry mass active content of 76% and processed in the same way as described above for the Si-FLG composite with a comparable coating mass.

The slurries are vacuum degassed under static vacuum for 1 hour. Anode coatings are cast onto 10 µm thick Cu foil (Oak Mitsui, electrodeposited) using an RK printing applicator (RK Instruments Ltd) with a partial vacuum applied to the Cu foil and a doctor blade set at a blade gap of 100 µm. Coated electrodes are dried on a hot plate at 80 ^{o}C followed by vacuum drying (7 mBar) for 12 hours at 70 ^{o}C. Hohsen 2032 coin cells were used for charge-discharge cycle testing versus Li metal (MTI Corporation, purity = 99.9%). All cells used a GF/A separator rather than a porous polyolefin separator. The electrolyte used was EC: EMC (3: 7), with 15 wt% FEC and 3 wt% VC. The cycling voltage range was 0.005 to 1.0 V. The first (formation) cycle used a relatively low current (± C / 25), followed by higher currents on subsequent cycles (± C / 5). Differential plots of dQ / dV were calculated directly from the data.

FLG Anode Formulation

To establish the contribution of the FLG to overall reversible capacity, an electrode was formulated based on a composition of 76: 14: 10 dry mass proportions of FLG: Na-PAA and carbon black. 4 grams of FLG (XG Sciences) is mixed with 8.65 grams of C-mix slurry (10.5 wt %) in a Nalgene vessel. The slurry mixture is initially blended with a spatula for 5 minutes and then subjected to ultra-sonication for 10 minutes to disperse any carbon agglomerates. 6.84 grams of partially neutralized Na-PAA solution (11.7 wt %) is added to the resulting slurry, and then it is further dispersed with a Primix Homodisperser Model 2.5 for 30 minutes. Afterwards, the composite slurry is transferred to a Filmix mixing vessel and subjected to the following mix cycle: dispersed for 30 s at 10 m/s then 30 s at 25 m/s.

The slurry is cast onto 10 µm Cu foil using a drawdown coater (RK Instruments Ltd) with a blade gap of 100 µm. Coated electrodes are dried on a hot plate at 50^{o}C followed by vacuum drying (7 mBar) for 12 hours at 70^{o}C.

Electrochemical characterisation

Charge-discharge cycle testing was carried out with a constant current-constant voltage charging (CC-CV) procedure. Cell testing was performed with a Maccor Potentiostat, with the cells housed in temperature-controlled conditions maintained at 25^{o}C.

BET Surface area & pore size distribution measurement

Surface area and porosity analysis was performed on a Micromeritics Gemini V surface area analyser Nitrogen sorption was carried out at 77 K on samples previously outgassed at 150ºC for 24 hours in a Micromeritics Flowprep 060 unit. The samples were then transferred to a Micromeritics V Surface Area and Pore Size Analyzer for analysis.

X-ray Diffraction

Crystallographic characterisation was performed using a PANalytical Empyrean XRD Diffractomer with Co anode, K_{α}0.1789nm operated at 40kV and 40mA over a scan range of 10 – 60 ^{o} at 1^{o}/min.

Raman Spectroscopy

The micro-Raman spectra were recorded on a Renishaw InVia Raman spectrometer integrated with a Leica optical microscope. A laser line of 532 nm was selected as excitation source and operated below 1 mW in order to avoid any local heating. The excitation was performed through a 50X objective (0.75 NA) giving a laser spot size of 0.86 µm and a 1800 grooves/mm grating resulted to a spectral resolution of ~ 2 cm^{-1}.

Transmission Electron Microscopy

Transmission Electron Microscopy (TEM) micrographs were obtained with a JEOL 2000FX instrument operated at 200 kV. The samples were dispersed in tetrahydrofuran (THF) under ultra-sonication and a droplet was placed on a carbon-coated copper TEM grid.

Results and Discussion

Material and Electrochemical Characterisation

The Si-FLG composite anode materials are characterised by FE-SEM. As shown in Figure 3**,** the Si microparticles, FLG and carbon additives are distributed well within the electrode material and together formulate quite a porous architecture. These carbon networks represent effective anode "wiring" and ensures maintenance of good electrical connection networks between active particles down to the Cu current collector. It can be observed from the SEM image that the sub-components of the anode's microstructure are multi-scale and hierarchical and this will benefit short and long-range electrical conductivity. The anode's porosity will allow effective permeation of electrolyte solvents to allow for a more uniform distribution of Li.

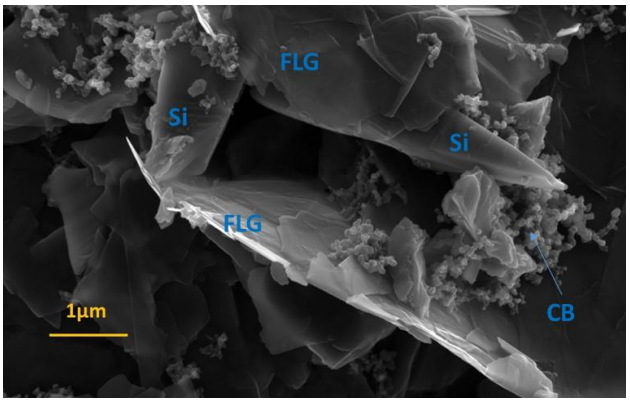

Figure 3 FE-SEM Si-FLG composite (CB = carbon black)

intercalated molecules, which are typically O-bonded functional groups and H_2O molecules[17].

Figure 4a outlines the crystallographic characterisation of the FLG by XRD. This gives information on the various structural properties of FLG, namely the interplanar distances of the lattices and the platelet thickness and the number of layers. The sharp peak at 30.7° indicates the 002 plane with the interlayer distance calculated as 3.38Å.

At higher 2θ reflections there are broader, less intense regions at 49.5°, 51.0° and 51.9°, corresponding to d-lattice spacing of 2.14, 2.08 and 2.05Å, respectively. In graphite this value is typically quoted as 3.35 – 3.36Å but the graphene layers differ in diffraction characteristics due to the structural defects, such as nano-holes and intercalated molecules, which are typically O-bonded functional groups and H_2O molecules [17]. Figure 4b shows the Raman spectra of the FLG with all the characteristic peaks of graphene. The D band at 1350 cm^{-1} is activated from the defects on graphene honeycomb structure and to the edges of the graphene layers. The intense peak at 1580 cm^{-1} (G band) is attributed to the bond stretching of the in-plane sp^2 carbon atoms while the overtone of the D band which is activated from a two-phonon scattering process is centred at 2720 cm^{-1} (2D band)[18]. The asymmetrical shape of the 2D band (inset)

and the large FWHM (71 cm^{-1}) together with the high I_G/I_{2D} ratio indicate that the material is a multilayer graphene consisting of at least 5 graphene sheets [19]. Figure 5 outlines the electrochemical testing of the electrodes in half cells (vs. Li). Fig 5a compares the first cycle charge-discharge voltage profiles for electrodes cycled to different capacity limits of 1200, 1800 and 3600mAh/g. The first (formation) cycle used a higher capacity limit than that adopted for subsequent charge-discharge cycling. This attempts to ensure sufficient amorphisation of the active material, such that further crystalline-to-amorphous transformation is avoided as much as possible within the fixed capacity cycling. The irreversible capacity loss on the first cycle (FCL %) for each cell is 19.1%, 18.4% and 27% respectively with the largest loss incurred at the full discharge capacity. Figure 5b and c compare the capacities and coulombic efficiencies during successive cycling of Si-FLG anodes at half and full specific capacity (1800 and 3579 mAh/g) against a Si anode containing no FLG. Whilst there is an initial decline in delithiation capacity from full lithiation to *ca.* 2000 mAh/g reversible capacity, there is a reasonably stable region of charge-discharge cycling to around 150 cycles. This can be attributed to effective interactions between the Si and FLG to give a structurally more stable electrode than is typically seen with only Si as the active material. This is demonstrated in profiles (iii) in 5b and c whereby a Si-only anode cannot endure more than 80 cycles at 2000mAh/g before the capacity fade becomes very pronounced with increasing cycle numbers. One possible explanation is that the more weakly connected particles now start to become fully isolated through an incremental breakdown of conductive networks and continued capacity fade.

This performance observation is supported by the coulombic efficiency data that clearly show a more profound efficiency decline in 5c (ii) and to a slightly lesser extent in 5c (i). Interestingly the efficiency begins to slightly increase in 5c (i) after *ca.* 150 cycles and according to Dahn[20] this may be attributable to the maturing of the SEI in this region of cycling with an associated slowing down of the parasitic reactions associated with electrolyte decomposition. The particles that remain in electrical contact with slowed SEI growth rate could be cycling more efficiently at this point.

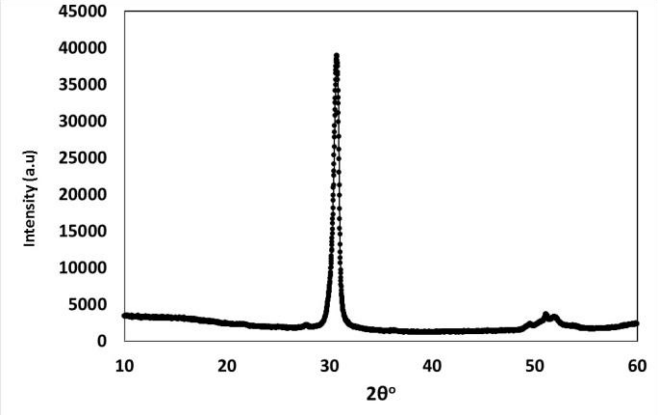

a.

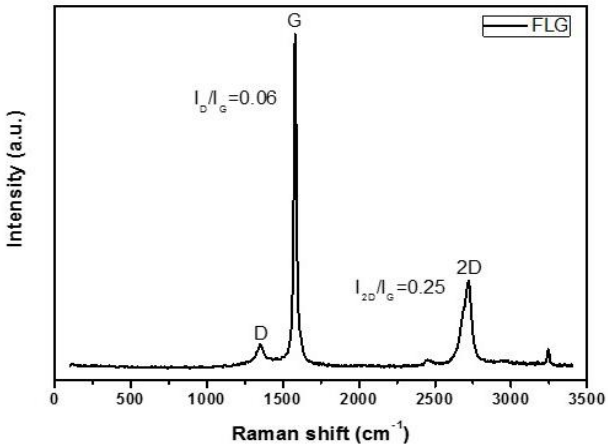

b.

Figure 4 a. X-Ray Diffractogram and **b**. Raman Spectrum of XG Sciences FLG nano-platelets.

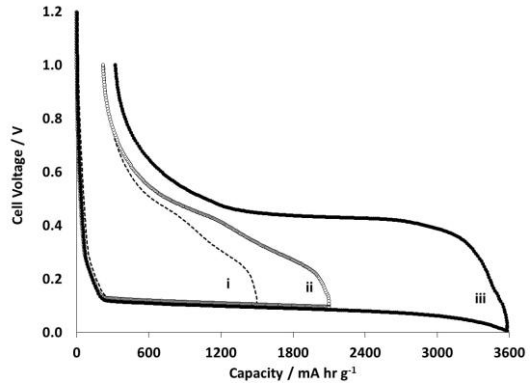

a.

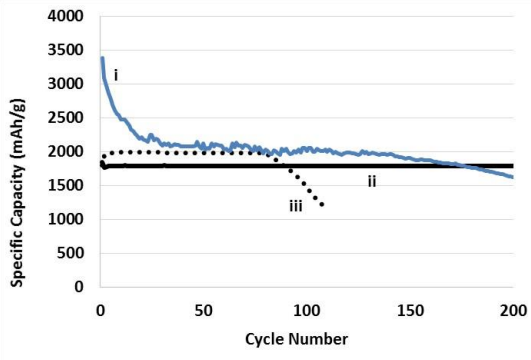

b.

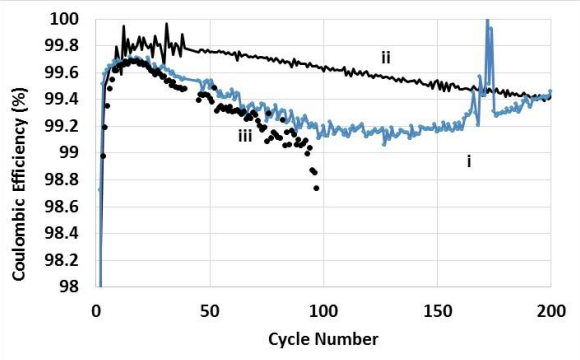

c.

Figure *5* a. Voltage vs. Capacity for Si-FLG Anodes at Capacities (i) 1200mAh/g (ii) 1800mAh/g (iii) 3579mAh/g **5 b**. Comparison of performance in coin cells vs. Li/Li^+ showing delithiation capacity as a function of cycle number for (i) Si-FLG anode (3579mAh/g), (ii) Si-FLG anode (1800mAh/g); (iii) Si only anode (2000mAh/g) (iii) . **c.** Coulombic efficiency vs. cycle number for (i) Si-FLG anode cycled at 3579mAh/g, (ii) Si-FLG anode cycled at 1800mAh/g and (iii) Si only anode cycled at 2000mAh/g.

An examination of the selected area electron diffraction (SAED) pattern provides further information of the layered structure. The inner diffraction ring of the (002) plane consists of a set of 12 (6 pairs) of intense diffraction peaks, and the rotation between the graphene layers is calculated to be 12°.

Firstly there is the interaction with the active material (as depicted in Figure 1), and it is reported that there are three different modes of binding that occur between expansive materials (such as Si) and polymers[21]: (i) particles are stuck together with a “flexible paste”; (ii) a flexible binder matrix is formed of covalent bonding between in which the active material is also covalently bound (via ester bond formation between the PAA-COOH and the Si-silanol groups; (iii) a similar embedded interaction exists but instead of covalent bonding there is a hydrogen-bonding network. This is stated to be advantageous as the bonds are non-permanent and thus able to break and reform as the Si particles move during expansion. The last mode of binding can only exist in polymers that contain hydroxyl groups. The partial neutralisation of the polymer using a sodium counter-ion induces chain extension by reducing inter- and intramolecular hydrogen bonding between carboxyl groups

(screening of electrostatic interactions). The flexibility of solvent selection with PAA also offers additional routes to electrode optimisation by allowing variable concentrations of polymer solution with a range of viscosities. Therefore, the polymer binder plays a key role in the retention of the electrode's microstructure stability for longer-term cycling. The electrochemical lithiation / delithiation behaviour of FLG resembles that of bulk graphite (whereas single layer graphene behaves dramatically differently) [22] and plays a key role in the retention of the microstructure stability for longer-term cycling.

Table 1 outlines the lithiation and delithiation processes that occur within graphitic carbon as a function of voltage and will be considered the same phases that occur in FLG materials.

Voltage	Lithiation / Delithiation Process
<0.9	a. Continued decomposition of electrolyte and formation of SEI b. $LiC_{72} \rightarrow LiC_{36}$
0.2 – 0.1	Formation of LiC_{27} and LiC_{18}
≈0.1	$LiC_{18} \rightarrow LiC_{12}$
0.1 – 0.25	$LiC_{12} \rightarrow LiC_{18}$
0.25 – 0.5	$LiC_{18} \rightarrow LiC_{36}$
0.5 – 1.0	$LiC_{36} \rightarrow LiC_{72}$

Table 1. Key lithiation stages within graphitic carbon

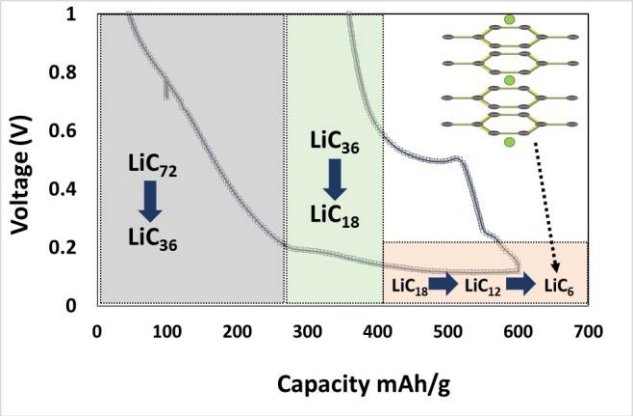

a.

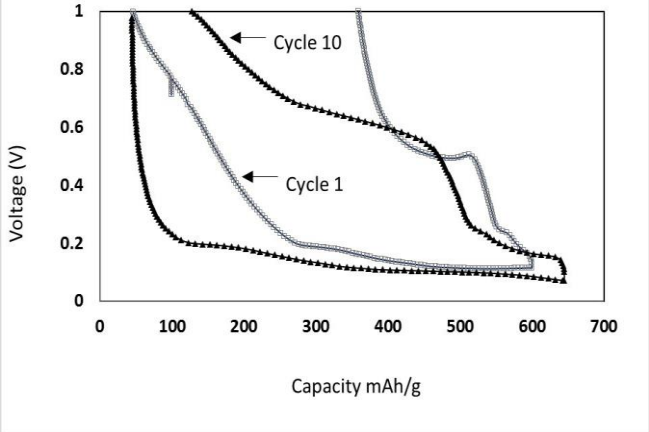

b.

Figure 6 a. Voltage vs. Capacity (mAh/g) 1st Cycle lithiation-delithiation of a FLG anode vs. Li. **b**. Voltage vs. Capacity (mAh/g) 1st and 10th Cycle lithiation-delithiation FLG anode vs. Li.

There are multiple slopes and plateaus in graphitic carbons, each representing a lithiation or delithiation process summarised by the reaction schemes in Table 1 [23]. The specific surface area of the FLG is measured as 123 m^2/g and constitutes a large substrate to accommodate electrolyte decomposition and surface reaction of Li species. The voltage profile of the FLG, unlike that of artificial and synthetic bulk graphite materials, is quite sloped and does not

display the classic plateaued profile of layered carbon. Interestingly the type of slope is similar to that seen in hard carbon materials and is ascribed to the disordered crystal structure. Hard carbon materials can contain significant quantities of nano-scale porosity, which can be modelled by a series of graphene sheets arranged like a so-called "house of cards" where a proportion of the particles comprise of two or three stacked layers and constitute lithium insertion sites[24]. In the case of FLG carbon these stacked layers represent the majority of the material and will vary in layer number, size and chemical environment resulting in the capacity developing over a range of potentials to generate a "sloping" voltage profile**.** When comparing cycles 1 and 10 in Figure 6b it is evident that there is a significant difference in capacity loss 60% on the first cycle but this reduces to 15.9% on cycle 10. The formation of SEI, especially on high surface area materials such as FLG, is a major contributor to early capacity loss but is not the entire story. The electrolyte additives used in this study were selected to promote a more stable SEI on the Si and reduce its dynamic breakdown and reformation. The effectiveness comes from the formation of fluoride ions from electrolyte breakdown, which leads to the chemical attack of any Si-oxide surface passivation layers subsequently forming a kinetically stable SEI that is based predominantly on lithium fluoride and lithium oxide. See Equation 1. Previous work has also indicated that polycarbonates such as polymeric fluorocarbonate and vinylene carbonate (VC) are formed during the reduction of FEC and also serve to stabilise the SEI.

Xu *et al* [25] extend the claims to FEC acting to prevent particle agglomeration, cracking and influencing the salt dissolution reaction. However, it is unlikely that any layer of inorganic, organic or combined species formed can contain the expansive forces that lead to individual Si particle cracking. The effectiveness of FEC in improving the coulombic efficiency and capacity retention has been investigated by Schroder *et al* [26]. There is a clear shift in the shape of the voltage profile during the lithiation phase of cycle 10. The voltage descends far more steeply and the plot has a more distinctive plateau at voltages below 0.1V. Figure 7a shows the DFT pore size distribution and specific surface area (as calculated by BET method) for the FLG nano-platelets. Figure 7b shows an FIB prepared cross-section of an electrode coated using FLG and PAA (refer to Section 2.4 for formulation details). The multiple layers are easily identifiable and the coating structure is very porous and will allow good permeation of electrolyte solvents. The largest

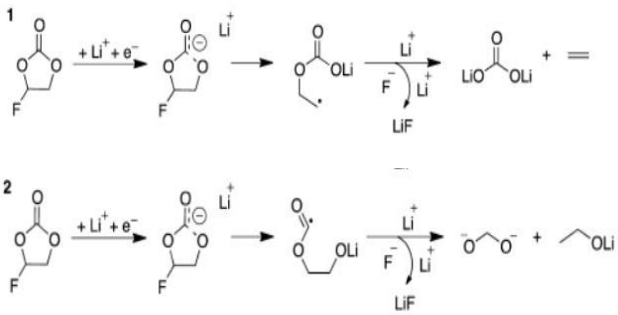

Equation 1. Electroreduction of fluoroethylene carbonate to lithium fluoride. **2**: electroreduction of fluoroethylene carbonate to form lithium fluoride methylenedioxyl ion or carbon dioxide and lithium ethoxide [26].

incremental pore volume is attributable to 34-37 nm pore widths and represents >50% of the cumulative pore volume, with *ca*. 80% of the total pore volume being found in pores greater than 30 nm. Further smaller distributions are observed centred at 15, 9 and 1.5 nm, accounting for the remaining pore volume. This pore structure spans both the micro and mesoporous scale, with the higher mesoporous contribution ensuring maximum electrolyte

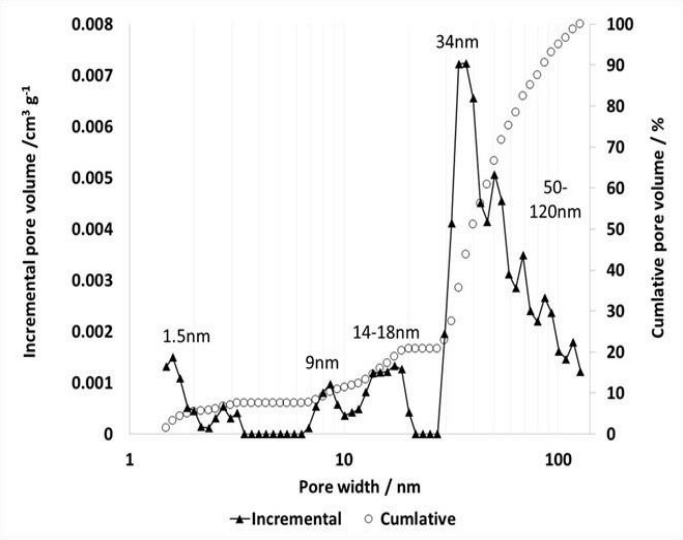

a.

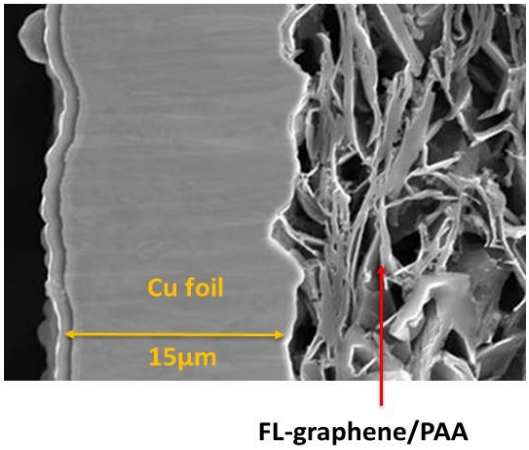

b.

Figure 7a. Density Functional Theory (DFT) pore size distribution and surface area measurement for FLG nanoplatelets **b.** FIB section of a FLG nanoplatelets-based anode coating.

wetting and diffusion of electrolyte species throughout the material and maximum utilisation in cycling. The polydispersed nature of the Si particles used in this study are observed in Figure 8, with a D_{50} of 2.92µm but the particle size range extends to around 20µm for a smaller volume % of the material. This is quite a common phenomenon with metallurgical powders that have any grinding or milling stages within their manufacture.

This this broad particle size distribution can impact the local chemical and electrical behaviour of a porous anode. Firstly it has been demonstrated using simulations based on computer-generated electrode microstructures that broad particle size distributions can deliver up to twice the energy density of monodispersed particles[27].

However, electrodes based on monodisperse particle size distributions deliver the highest combined energy and power density due to a higher surface area of active material per unit volume[27].

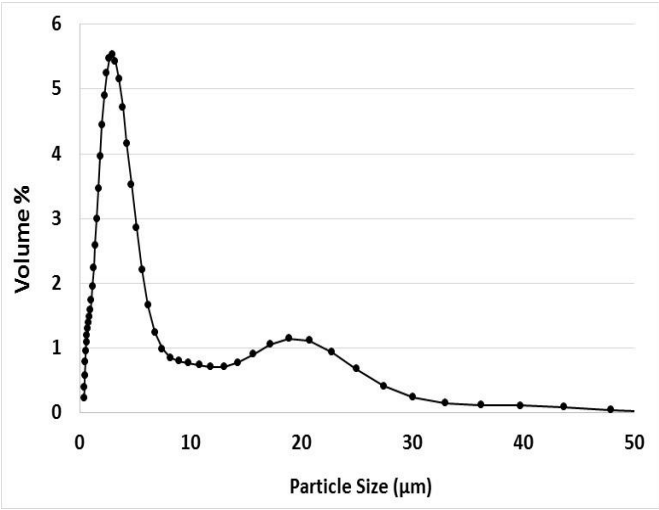

Figure 8 Particle Size Distribution of micro-sized Si particles.

Differential Capacity Characterisation

(i) Si-FLG Composite dQ/dV Evaluation.

Figure 9a**.** shows the differential capacity (dQ/dV) plots for cycle 2 – 10 in the potential range 0 – 1V to a capacity of 3579 mAh/g, showing information about structural transformations during lithiation and delithiation for Si-FLG anodes vs. Li/Li^+ in a half-cell. The profiles show characteristic Si lithiation processes with the 1st lithiation being distinctly different to subsequent lithiation processes due to the dominant conversion processes that transform crystalline (c-Si) to amorphous silicon (a-Si).

During the discharge process three peaks are observed at:

(i) The 1st discharge process between 0.25-0.3V appears as quite a broad doublet peak that possibly indicates a two-stage gradual lithiation of the a-Si lattice to form a-$Li_{2.0}Si$ (see process 1 in Figure 7a.) According to Grey *et al* this phase is still composed of extended Si networks and large Si-Si clusters [28]. It has also been reported elsewhere that doublet or split peaks within discharge dQ/dV peaks can be attributed to non-uniform lithiation events or intermediate phases[26].

(ii) The second discharge process occurring at 0.09-0.1V corresponds to the formation of $Li_{3.5}Si$ and is recognized as the further breaking of Si-Si bonds to form small Si clusters and eventually isolated Si atoms [28]. On cycle 2 only there is a small peak around 50mV which has been reported to correspond with the formation of *c*-$Li_{3.75}Si$ from *a*-Li_xSi [28–30].

(iii) During the delithiation processes two single peaks are observed at 0.45V – this corresponds to the transformation of the lithium-rich c-$Li_{3.75}Si$ phase and partially delithiated / more defective c-$Li_{3.75}Si$ crystalline phase, to amorphous lithium silicide *a*-$Li_{2.0}Si$[26].

(iv) The delithiation at 0.27 V corresponds to the delithiation of *a*-$Li_{\sim 2.0}Si$ / *a*-$Li_{\sim 1.1}Si$.

Figure 9b compares the differential capacity plots for lithiation-delithiation cycles 2-10 and 91-100. Whilst the dQ / dV peak at 0.25 V occurring during lithiation consistently splits into a double peak in the first 10 cycles, it is no longer evident approaching cycle 100.

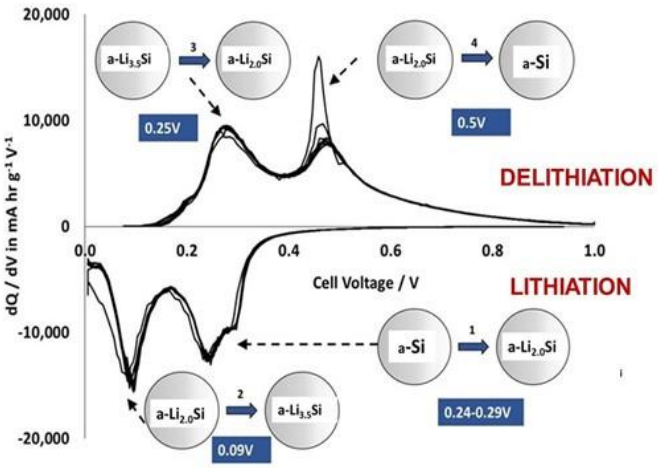

a.

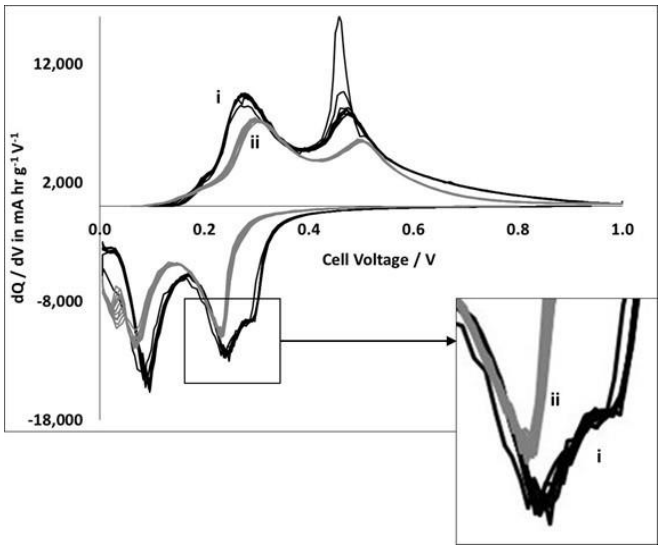

b.

Figure 9. Differential Capacity (dQ/dV) as a function of cycle

numbers **a**. dQ/dV Plot Si-FLG cycle number 2 – 10, **b**. (i) 2-10 and (ii) 91-100.

Over increasing cycle numbers up to 100 there is an obvious gradual reduction in the peak intensity during delithiation as a function of cycle number. Additionally, there is a shift in the profiles' peak voltage towards lower values during lithiation, suggesting increasing resistance with higher cycle number as the cell is challenged to reach capacity.

This reflected in the dQ/dV plot by way of a much reduced peak height resulting from the lower available capacity as a function of cycle number.

The wider peak-peak separation reflects an increase in electrode resistance and this will continue to build up as a result of continual SEI growth on the Si, a proportion of electrically isolated active particles from breakdown in the connective C-network, but also from areas where an onset of delamination occurs of the electrode coating from the separator. After 100 cycles the area beneath the lithiation peaks continues to decrease until these peaks essentially flatten at 170 cycles where the capacity retention has reduced considerably.

Few Layer Graphene Electrochemical Evaluation

Figure 10a compares the differential capacity curves of FLG anode vs. Li during the 1st, 2nd, 4th and 10th charge-discharge cycle in profiles i - iv. In cycle 1 and 10 lithiation peaks occur at 0.19, 0.17 and 0.12V with subsequent delithiation events taking place within 2 broad sets of voltage range (0.1-0.3V and 0.5-0.7V). There are peak shifts during cycles 1- 10 when delithiation processes occur with broad peaks developing during the 4th and 10th cycle.

Lithiation peaks display more of a consistent overlap than the corresponding delithiation peaks, which display more divergence and increasing voltage separation between delithiation events as a function of cycle number. This suggests a shifting energy requirement to remove Li from the graphene structures as a function of increasing cycle number. Figure 10b shows the delithiation capacity (mAh/g) as a function of cycle number for an anode with FLG as the total anode active material vs Li in a half-cell cycling test.

The anode is capable of reversible lithiation to capacities of >500mAh/g for ≥ 100 cycles in a non-optimised anode formulation, with a discharge capacity retention of 92.5% at cycle 100 Therefore, in addition to enhancing the conductivity of the composite film and introducing any improvements to the tensile properties of the Si-based anode, the FLG can also contribute to the

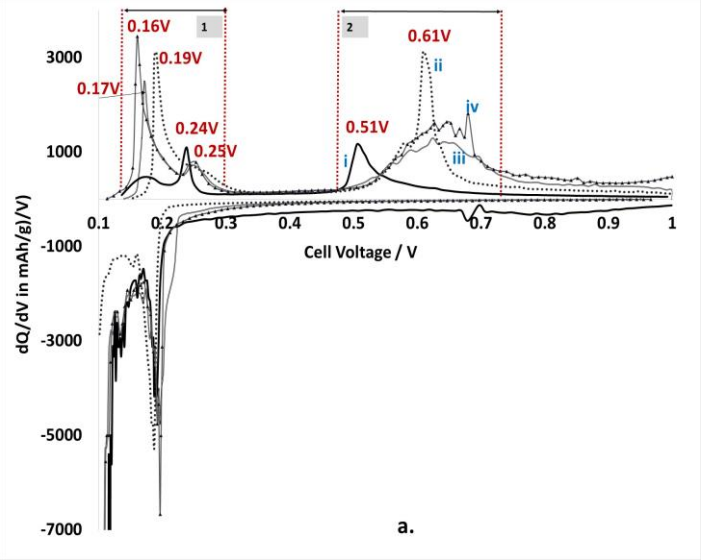

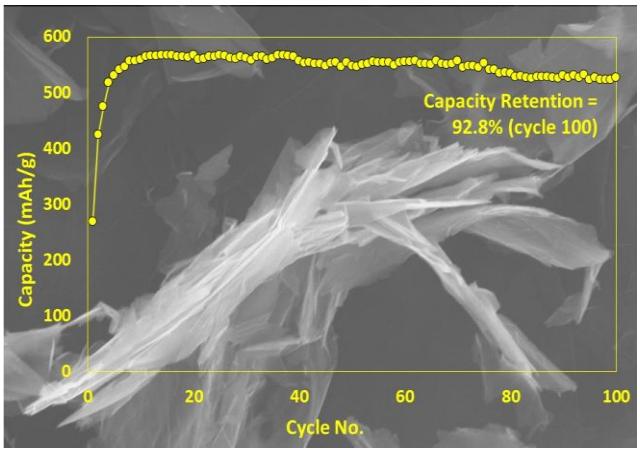

b.

Figure 10 a. Differential Capacity Analysis of discharge capacities of FLG anode vs. Li (i) Cycle 1 (ii) Cycle 2 (iii) Cycle 4 and (iv) Cycle 10. **b**. Delithiation Capacity and Coulombic Efficiency (%) vs. Cycle No. of FLG anode vs. Li.

reversible capacity to a higher level than is possible with bulk graphite (372mAh/g). It has been reported that in Si-only anode films the continual large volume changes that accompany the charge-discharge process leads to the agglomeration of the Si [31]. This in turn causes destructive microstructural changes that result in the gradual breakdown of the conductive network down to the current collector with concomitant capacity fade. It is therefore a possibility that the presence of a significant amount of FLG can influence this phenomenon beneficially.

Conclusions

This investigation shows the enriched electrochemical performance of silicon anodes that incorporate few layer graphene in addition to conventional carbon additives. Reasonable reversible lithiation behaviour is achievable at 1800 and 2000 mAh g^{-1} (with the hybrid system out-performing an anode based only on a Si active mass but there is a requirement to continue to improve the coulombic efficiency of these anode systems, especially as larger format cells are developed with long-term cycling requirements. Further improvements can also be made by optimising the ratio of the Si and FLG. The high capacity durability over hundreds of cycles of these anode systems derives from improving multiple cell components in unison. FLG contributes to the reversible capacity, showing reasonable electrochemical behaviour as a single active material, demonstrating reversible capacities of almost 600 mAh/g. The inclusion of FLG is also likely to be enhancing the tensile strength of the electrode but to confirm this requires further measurement and characterisation. Poly (acrylic acid) incorporating a Na-counter ion to extend its chain configuration, is an effective binder to generate a stable electrode architecture capable of

enduring volume expansion and particle movement for *ca.* 200 charge-discharge cycles. There is scope to further investigate what constitutes the optimal Si-FLG ratio for this type and particle size of Si and improve the electrode stability and performance even more.

Using dQ / dV analysis some interesting features, particularly at higher capacities, are seen. During lithiation, there are two main stages; break-up of the amorphous silicon structure to form large clusters, and then further break up to small clusters and isolated silicon atoms. The proportion of the total lithiation charge on the small clusters / isolation stage usually decreases during initial cycles, but can then increase again. With further optimisation of the electrode formulation and further testing in full cells there is development opportunity for an inexpensive route for making a durable anode capable of being reversibly cycled to capacities much higher than that of current graphite technologies.

Acknowledgements

This work was supported by the High Value Manufacturing Catapult (RESWM8053) at the University of Warwick's Energy Innovation Centre.

References

1 D. Ma, Z. Cao and A. Hu, *Nano-Micro Lett.*, 2014, **6**, 347–358.

2 L.-F. Cui, L. Hu, H. Wu, J. W. Choi and Y. Cui, *J. Electrochem. Soc.*, 2011, **158**, A592.

3 M. N. Obrovac and L. J. Krause, *J. Electrochem. Soc.*, 2007, **154**, A103.

4 J.-G. Ren, Q.-H. Wu, G. Hong, W.-J. Zhang, H. Wu, K. Amine, J. Yang and S.-T. Lee , *Energy Technol.*, 2013, **1**, 77–84.

5 X. H. Liu, L. Zhong, S. Huang, S. X. Mao, T. Zhu and J. Y. Huang, *ACS Nano*, 2012, **6**, 1522–1531.

6 A. Magasinski, B. Zdyrko, I. Kovalenko, B. Hertzberg, R. Burtovyy, C. F. Huebner, T. F. Fuller, I. Luzinov and G. Yushin, *ACS Appl. Mater. Interfaces*, 2010, **2**, 3004–10.

7 S.-L. Chou, Y. Pan, J.-Z. Wang, H.-K. Liu and S.-X. Dou, *Phys. Chem. Chem. Phys.*, 2014, **16**, 20347–59.

8 J. S. Kim, W. Choi, K. Y. Cho, D. Byun, J. Lim and J. K. Lee, *J. Power Sources*, 2013, **244**, 521–526.

9 J. Song, M. Zhou, R. Yi, T. Xu, M. L. Gordin, D. Tang, Z. Yu, M. Regula and D. Wang, *Adv. Funct. Mater.*, 2014, **24**, 5904–5910.

10 D. Chen, R. Yi, S. Chen, T. Xu, M. L. Gordin and D. Wang, *Solid State Ionics*, 2014, **254**, 65–71.

11 L. Luo, J. Wu, J. Luo, J. Huang and V. P. Dravid, *Sci. Rep.*, 2014, **4**, 3863.

12 L. L. Tian, Q. C. Zhuang, J. Li, Y. L. Shi, J. P. Chen, F. Lu and S. G. Sun, *Chinese Sci. Bull.*, 2011, **56**, 3204–3212.

13 B. Partoens and F. M. Peeters, *Phys. Rev. B - Condens. Matter Mater. Phys.*, 2006, **74**, 1–11.

14 I. Bloom, A. N. Jansen, D. P. Abraham, J. Knuth, S. a. Jones, V. S. Battaglia and G. L. Henriksen, *J. Power Sources*, 2005, **139**, 295–303.

15 I. Bloom, J. Christophersen and K. Gering, *J. Power Sources*, 2005, **139**, 304–313.

16 I. Bloom, J. P. Christophersen, D. P. Abraham and K. L. Gering, *J. Power Sources*, 2006, **157**, 537–542.

17 S. C. Jun, *Fundamental of Graphene*, Wiley-VCH verlag GmbH & Co. KgaA, 2015.

18 A. C. Ferrari, J. C. Meyer, V. Scardaci, C. Casiraghi, M. Lazzeri, F. Mauri, S. Piscanec, D. Jiang, K. S. Novoselov, S.

Roth and A. K. Geim, *Phys. Rev. Lett.*, 2006, **97**.

19 Y. Hao, Y. Wang, L. Wang, Z. Ni, Z. Wang, R. Wang, C. K. Koo, Z. Shen and J. T. L. Thong, 2010, 195–200. .

20 B. Gyenes, D. a. Stevens, V. L. Chevrier and J. R. Dahn, *J. Electrochem. Soc.*, 2014, **162**, A278–A283.

21 U. S. Vogl, P. K. Das, A. Z. Weber, M. Winter, R. M. Kostecki and S. F. Lux, *Langmuir*, 2014, **30**, 10299–10307.

22 E. Pollak, B. Geng, K. J. Jeon, I. T. Lucas, T. J. Richardson, F. Wang and R. Kostecki, *Nano Lett.*, 2010, **10**, 3386–3388.

23 J. Shim and K. A. Striebel, *J. Power Sources*, 2004, **130**, 247–253.

24 D. A. Stevens and J. R. Dahn, *J. Electrochem. Soc*, 2001, **148**, A803–A811.

25 C. Xu, F. Lindgren, B. Philippe, M. Gorgoi, F. Björefors, K. Edström and T. Gustafsson, *Chem. Mater.*, 2015, **27**, 2591–2599.

26 K. Schroder, J. Alvarado, T. A. Yersak, J. Li, N. Dudney, L. J. Webb, Y. S. Meng and K. J. Stevenson, 2015.

27 C. Erk, T. Brezesinski, H. Sommer, R. Schneider and J. Janek, *ACS Appl. Mater. Interfaces*, 2013, **5**, 7299–307.

28 K. Ogata, E. Salager, C. J. Kerr, a E. Fraser, C. Ducati, A. J. Morris, S. Hofmann and C. P. Grey, *Nat. Commun.*, 2014, **5**, 3217.

29 M. N. Obrovac and L. Christensen, *Electrochem. Solid-State Lett.*, 2004, **7**, A93.

30 M. T. McDowell, I. Ryu, S. W. Lee, C. Wang, W. D. Nix and Y. Cui, *Adv. Mater.*, 2012, **24**, 6034–41.

31 L. Ji, H. Zheng, A. Ismach, Z. Tan, S. Xun, E. Lin, V. Battaglia, V. Srinivasan and Y. Zhang, *Nano Energy*, 2011, 1–8.